Application of maximum entropy to extract Fermi surface topology from positron annihilation measurement

1994 J. Phys.: Condens. Matter 6 L435

(http://iopscience.iop.org/0953-8984/6/31/003)

J. Phys.: Condens. Matter 6 (1994) L435–L443. Printed in the UK

LETTER TO THE EDITOR

Application of maximum entropy to extract Fermi surface topology from positron annihilation measurement

S B Dugdale, M A Alam, H M Fretwell, M Biasini and D Wilson
H H Wills Physics Laboratory, University of Bristol, Tyndall Avenue, Bristol BS8 1TL, UK

Received 23 May 1994

Abstract. Over the past two decades or so, the positron annihilation technique has successfully probed Fermi surface (FS) topologies in a variety of metals and alloy systems. However, in electronically complex systems, due to the relatively weak FS signals compared with those arising from annihilations from a large number of full bands, possible strong positron wave function comes into effect. Here, we introduce a new way of looking at the problem using maximum-entropy enhancement of the data. Test results from the simple FS picture of vanadium are presented.

During the last decade or so, the technique of two-dimensional angular correlation of positron–electron annihilation radiation (2D ACAR) has been used increasingly with considerable success in the study of Fermi surface topology in metallic systems [1, 2]. The technique has proved particularly valuable in the investigation of disordered alloys or studies at higher temperatures where traditional quantum oscillatory methods are not applicable. In a 2D ACAR experiment [3] one measures the number of annihilation photons as a function of the angular deviations θ, ϕ (say in the x and y directions; z is the mean direction of photon emission) from anti-collinearity between the two emerging quanta (a few milliradians). These angles are directly proportional to the corresponding positron–electron momentum components p_x, p_y which produce these deviations. In these experiments, because of technical restrictions, p_z cannot be measured simultaneously and as a result the experimental data represent a projection of the underlying 3D electron–positron momentum density $\rho_{ep}(\boldsymbol{p})$

$$N(\theta,\ \phi) \equiv N(p_x,\ p_y) = \text{constant} \times \int \rho_{ep}(\boldsymbol{p})\, \mathrm{d}p_z. \tag{1}$$

Assuming that the positron is thermalized and that the positron and electron wave functions can be approximated by Bloch waves, $\rho_{ep}(\boldsymbol{p})$, in the one-electron model, is given by [3]

$$\rho_{ep}(\boldsymbol{p}) \equiv \sum_{kj} \sum_{\boldsymbol{G}} n_j(\boldsymbol{k}) \left|C_{\boldsymbol{G}j}(\boldsymbol{k})\right|^2 \delta(\boldsymbol{p} - \boldsymbol{k} - \boldsymbol{G}) \tag{2}$$

where $n_j(\boldsymbol{k})$ is the $\boldsymbol{k}$-space occupation density in the jth band, $\boldsymbol{G}$ is a reciprocal lattice vector and $C_{\boldsymbol{G}j}(\boldsymbol{k})$ is the Fourier coefficient of the electron–positron (Bloch) wave function product. The Fermi surface features appear as breaks in $\rho_{ep}(p)$ via the $n_j(\boldsymbol{k})$ values. The delta function indicates that these features will be redistributed in all zones since an electron with wave vector $\boldsymbol{k}$ will not only contribute at a measured momentum $\boldsymbol{p} = \boldsymbol{k}$ but also at

0953-8984/94/310435+09$19.50

$p = k + G$ with intensity $|C_{Gj}(k)|^2$ (the higher momentum components 'HMCs'). In the approximation where the positron wave function is a constant and the $C_{Gj}(k)$ values are independent of k (or at least only a slowly varying function of k), the contributions from the higher zones can be summed to that around $G = 0$ (LCW, reference [4]) to reconstruct the k-space density whose breaks define the Fermi surface. The usual procedure to elucidate FS topologies from 2D ACAR involves correcting the raw data with a 'momentum sampling function' [5] to correct for the fact that with finite-size detectors, the probability of measuring all angles is not unity. Such functions are calculated from single-detector responses and needs to be done for each experiment. The LCW procedure is then applied to this corrected (and often folded around symmetry axes to improve statistics) data.

As in any experimental situation the data contain artefacts of the measurement procedure. In 2D ACAR experiments the following have to be considered. First of these is the instrumental resolution function arising from: (i) the intrinsic resolution of the position sensitive detectors (Anger Cameras [5]) used to detect the locations of the two annihilation photons in space; (ii) the size of the positron source image on the specimen which defines the origin of the frame of reference in which the angles between the photons are defined; and (iii) the positron thermal momentum [3]. Secondly, the positron being a charged probe, exerts a certain perturbation on the electronic system which it samples. Both positron wave function and electron–positron many-body effects can significantly affect $\rho_{ep}(p)$. However, both the positron wave function and the many body effects enhance the probability of annihilation with the outer, less-tightly bound and polarizable electron states and neither can shift the breaks in $\rho_{ep}(p)$ that mark the Fermi surface [3, 6]. However, in some complicated systems, if the positron samples a large number of bands and only a small fraction of these contribute to the Fermi surface, the corresponding breaks in $\rho_{ep}(p)$ will be weak. If, in addition, the positron wave function is not a constant (2) and the $C_{Gj}(k)$ values are strongly k dependent, then LCW folding may produce unreal FS-like features (e.g. in the case of YBaCuO [7]). During the last year or so there have been efforts to improve the data analysis procedures, in particular with the view to enhance and/or isolate the expected 'sharp' breaks at the Fermi surfaces. If an appropriate way of enhancing the Fermi surface breaks can be found, one can also hope that some spurious features arising from positron wave function effects, which may be introduced in the measured spectra, will not be enhanced in the same way as the FS breaks so that Fermi surface topologies can be extracted for the most complicated materials. Recently, we have applied the technique 'Maximum Entropy' (MaxEnt) to $\rho_{ep}(p)$ obtained through 2D ACAR measurements in an effort to deconvolute (without having to solve the 'inverse' problem) the resolution function and thereby enhance the edge effects at the Fermi surface breaks. The technique is still under further development and, here, we present some preliminary results of such an exercise for vanadium and point out some advantages of such analysis. In a parallel effort, the University of Texas at Arlington group (West *et al* [8]) has developed and employed the so called 'band-pass' technique for edge enhancement with considerable success.

The idea behind this exercise is schematically described in figure 1. In the ideal 3D k-space the Fermi surface is defined by a sharp step in the occupation density $n(k)$. In the measured spectrum, this break is smeared by the resolution function, as shown by the, say, black curve. After the MaxEnt procedure, if we have enhanced the breaks to move closer to the ideal case (say, the grey distribution), then the difference curve should go through zero at the Fermi edge and such difference distributions should highlight the edge effects. The zero crossing principle will be strictly valid in the case of a 3D distribution. Due to integration, in a projected 2D ACAR picture the breaks will be less sharp, except in the case of a 'hole' Fermi surface if it is projected onto itself, where the distributions

will resemble those shown in figure 1. Whether features created by positron wave function effects would also be enhanced in the same way cannot be ascertained without carrying out proper band structure calculations, but one would intuitively hope that these would be of longer range, relatively smoothly varying and not contain such sharp breaks as at the FS. If that is true, then such difference curves would have eliminated the positron wave function effects at least partially, and such analysis would prove significant in positron studies of Fermi surface topologies.

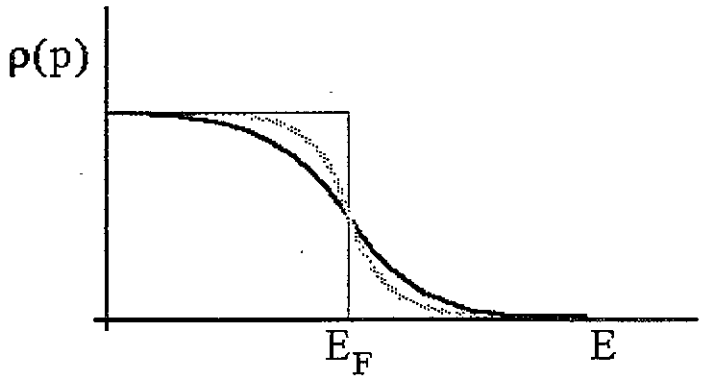

Figure 1. Fermi step function smeared by resolution (black) together with the enhanced version.

The method of MaxEnt is based on the following principle. Our experimental 2D data array is given by $\rho_{ep}(p_n)$, where p_n is the number of photons in a given pixel defined by (θ, ϕ). p_n is the probability that an electron–positron pair will annihilate to produce two photons with an angular deviation (θ, ϕ). The statistical nature of the whole matrix can be shown to be defined by [9]

$$S = -k\Sigma p_n \ln(p_n) \qquad n = 1 \text{ to } N. \tag{3}$$

Here, k is an arbitrary constant. This equation has the same form as the thermodynamic entropy. The true randomness of the data undergoes some kind of 'smoothing' due to the convolution of the experimental resolution function. This true randomness can be restored by taking the solution where this 'entropy' is maximized subject to the constraint of being consistent with the data. The method of MaxEnt [9] today is a fairly well established and widely used prescription for data enhancement. In this exercise, the entropy is maximized in a method based upon the so called 'Cambridge Algorithm' [10]. The consistency test is carried out via the chi-squared (C) test such that $C = \Sigma(D_k - F_k)^2/\sigma_k^2$, where F_k are the (trial) solutions, D_k the data, σ_k^2 is the variance of datum k. Details of the procedure can be found in [10]. In our analysis, we have applied MaxEnt both on corrected and folded as well as uncorrected data followed by a variety of trial analysis.

The 2D ACAR experiment on vanadium was carried out using the Bristol–Bologna spectrometer currently based in Bristol. Vanadium was chosen as the trial specimen due to its strongly anisotropic momentum density and fairly well known FS topology. The specimen was oriented such that the integration direction (p_z) was along the ⟨110⟩ and the resolved directions were ⟨110⟩ (p_x) and ⟨100⟩ (p_y). The raw spectrum contained 2×10^8

counts (i.e. 8×10^8 counts in the folded spectrum) in an array of 256×256 data points with channel widths of 0.1348 mrad in each direction.

In figure 2 we present contour plots of the corrected (with momentum sampling function) and folded 2D CAR spectra for vanadium (V) before 2(b) and after 2(c) MaxEnt enhancement together with the schematic Fermi surface topology for group VA metals 2(a). In the central area of the spectra the region of holes around the Γ and particularly the N points (see figure 2(a) for these symmetry points) are visible in the unenhanced picture (figure 2(b)) which are substantially enhanced in the MaxEnt distribution (figure 2(c)). Similarly, features in the higher momentum regions (towards the outer areas of the picture) are also enhanced. For comparison we reproduce the calculated (independent particle model) electron–positron momentum density by Matsumoto and Wakoh [11] for the same projection in figure 2(d). There is substantial agreement between figures 2(c) and 2(d) in the anisotropies arising from the various projections of the Fermi surface sheets around N and H points. The enhanced experimental distribution has far better agreement with the theoretical picture compared to the raw spectrum of figure 2(b). This gives confidence in the deconvolution procedure obtained through the MaxEnt prescription. The agreements extend into higher Brillouin zones (BZ). There are some residual differences between the enhanced experimental distribution and the calculated distribution, particularly around the Γ point. This can arise from a number of sources: (i) the error in the estimation of our combined resolution function; (ii) the smearing arising from the interpolations carried out in the theoretical distribution (the calculations were carried out using a k-grid ~3.5 times coarser k than in our experiments) and (iii) positron–electron many-body effects (the theory is IPM).

Figure 3(a) depicts the LCW folded k-space distribution from the unenhanced projection of the $\rho_{ep}(p)$ (i.e. the distribution in figure 2(b)) together with the projection of the first Brillouin zone. This shows the expected resemblance of the FS features shown in figure 2(a). A comparison of this projected 'k-space' picture with the difference distribution between the corrected, centred and folded spectrum (projected $\rho_{ep}(p)$) and its enhanced version (enhanced–raw) is noteworthy (figure 3(b)). As mentioned earlier, the FS breaks are expected to be highlighted in the difference distribution and it is interesting to note that all the FS related features observed in figure 3(a) are also clearly seen here, particularly those around the N-pockets. In figure 3(b), repetition of the features in the first BZ are also observable in the higher zones. As mentioned earlier, the difference distribution is expected to contain zero crossing points at the FS edge. This is indeed found to be the case at the N-pockets. We also applied the MaxEnt prescription on the raw (uncorrected and unfolded) spectrum. More remarkably, the difference distribution (enhanced–raw) again displays all the features observed in figure 3(b).

According to the assertions made earlier, in principle figure 3(b) largely contains the breaks representing the FS distributed over all zones. Therefore, an LCW folding here would also reproduce the full (projected) FS topology. Such a folded distribution is shown in figure 4(a). This is similar to that of the LCW folded distribution derived from the corrected, centred and folded 2D ACAR distribution shown in figure 3(a) with some subtle differences. The features around the N_N-pockets are somewhat different in shape and the 'lobes' around the hole region surrounding the $N_\Gamma N$ point along the ⟨110⟩ direction (figure 2(a)) are more clearly shown. Along the ⟨100⟩ direction the 'lobes' are somewhat obscured but still visible. For comparison, in figure 4(b) we present a picture of the LCW folded version of the theoretical distribution of Matsumoto and Wakoh. There are many more similarities between figures 4(a) and 4(b) than either between figures 3(a) and 4(a) or between 3(a) and 4(b). The hole pockets around N in figure 4(a) are much more akin in

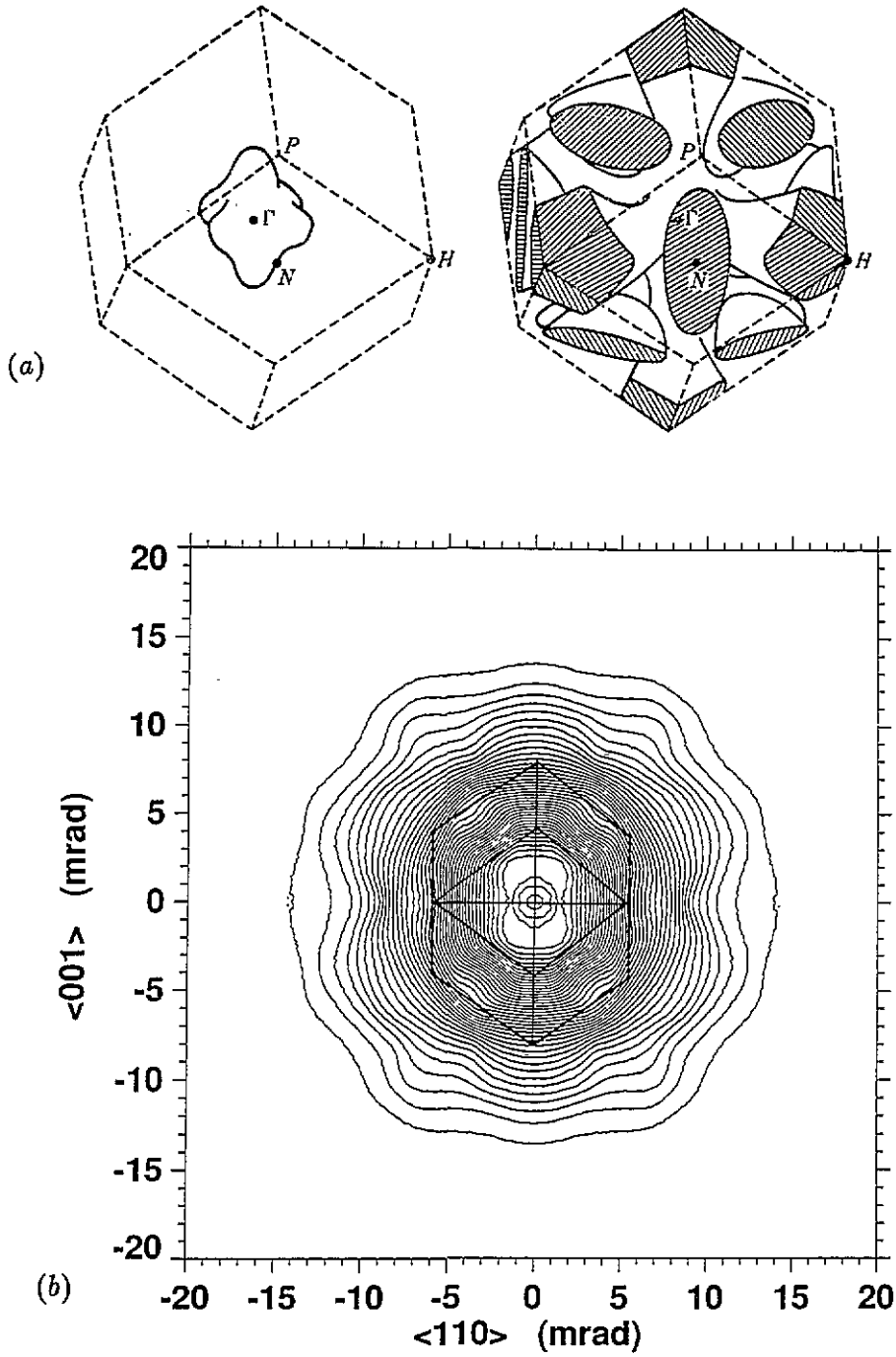

Figure 2. (*a*) Schematic representation of the Fermi surface features of V. The left hand picture shows the Γ-centred hole octahedron. The right hand picture shows the ellipsoidal hole pockets at *N* and jungle-gym arms in [100] directions. (*b*) 2D ACAR spectrum after correction and folding as described in the text. The straight lines show the outline of the projected first BZ. (*c*) The spectrum in part (*b*) after MaxEnt enhancement. The straight lines show the outline of the projected first BZ. (*d*) Theoretical *p*-space density by Matsumoto and Wakoh [11] integrated along the same direction as in parts (*b*) and (*c*).

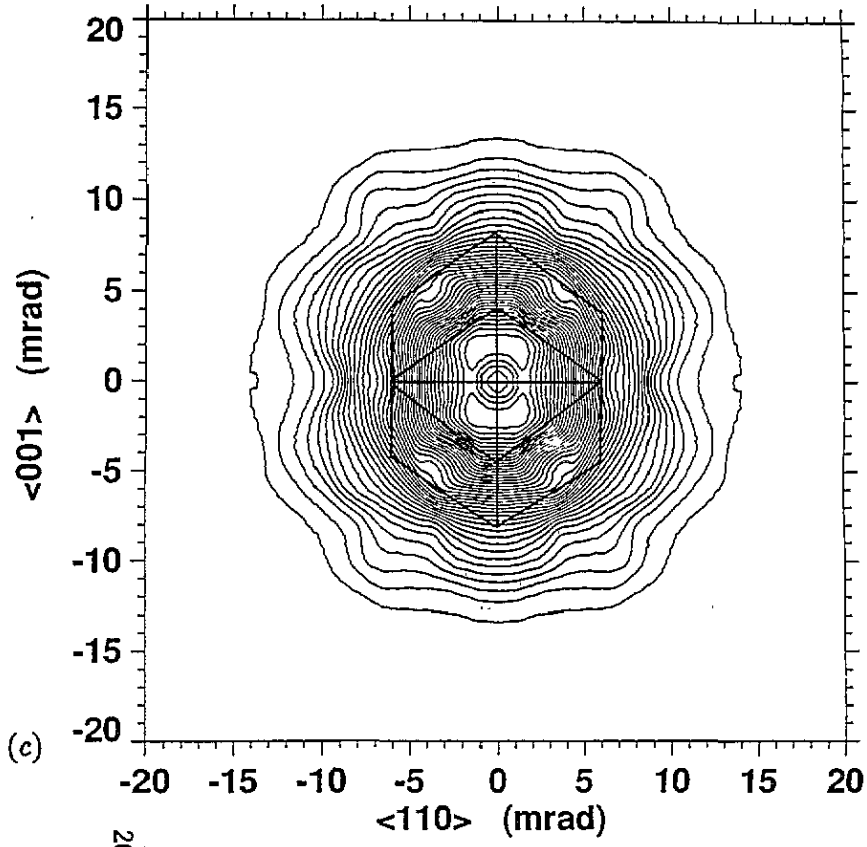

(*c*)

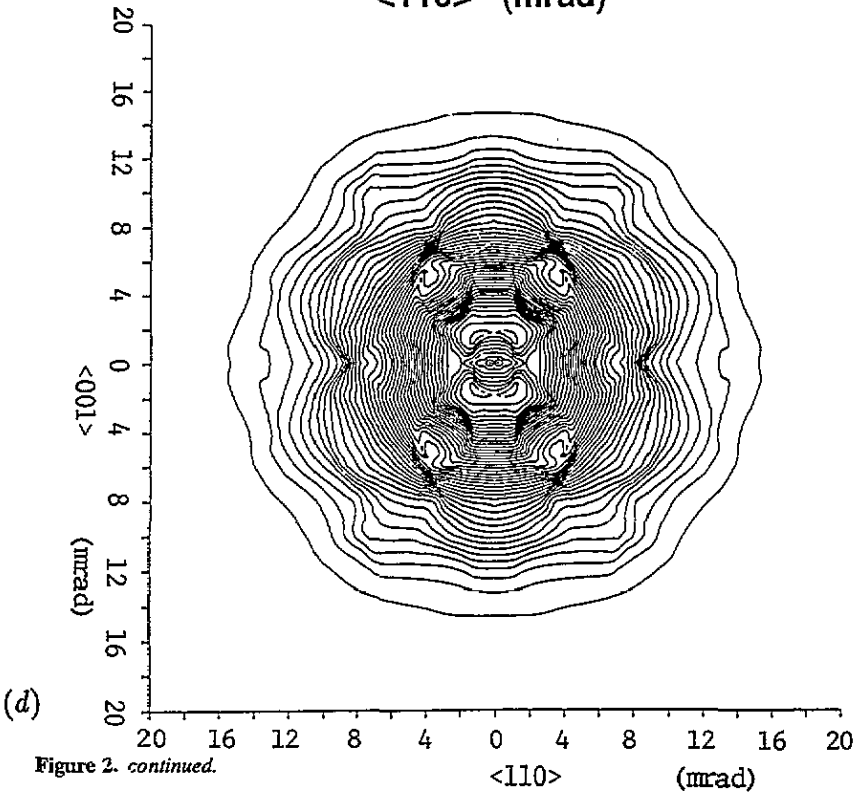

(*d*)

Figure 2. *continued.*

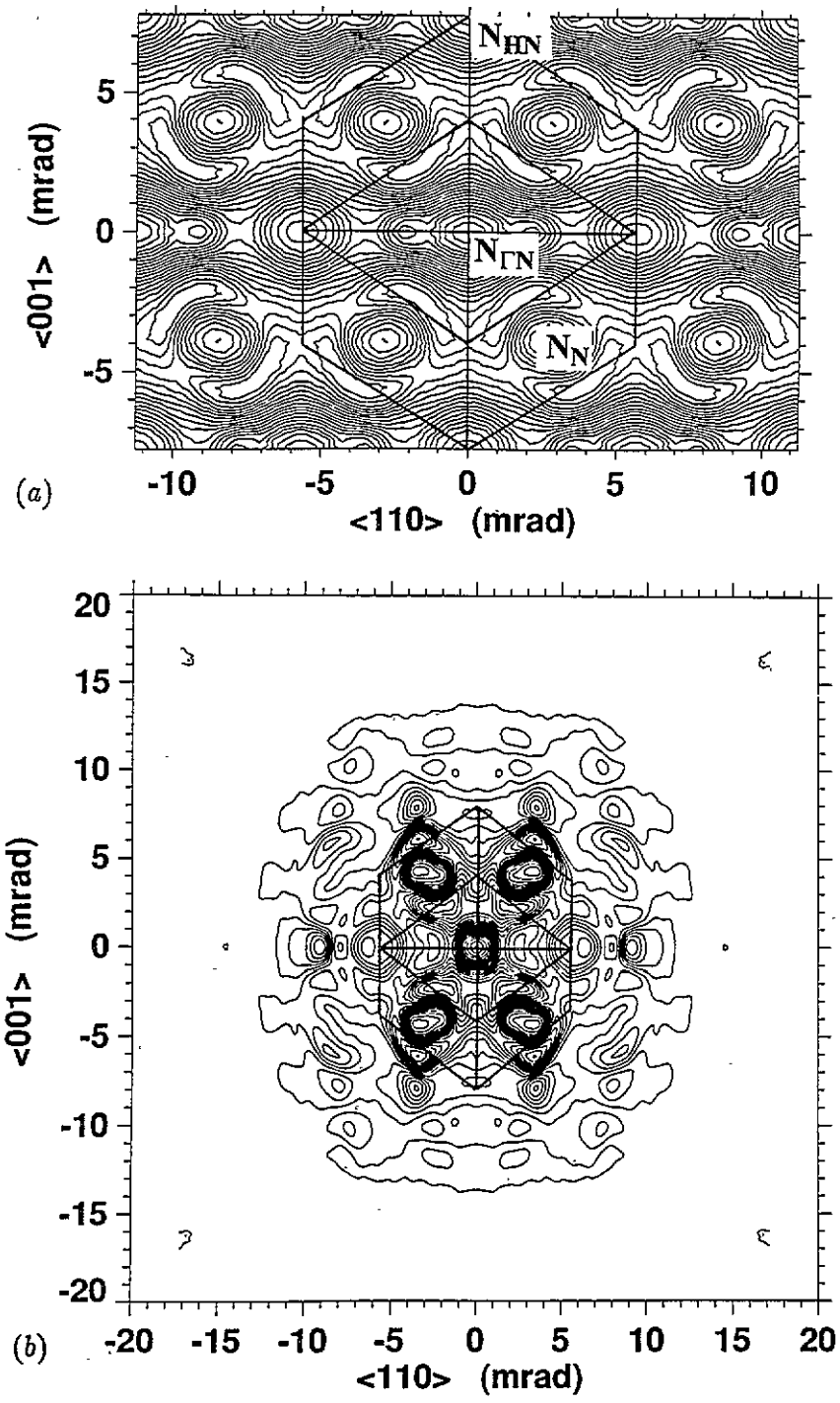

Figure 3. (*a*) Integrated (along 110 direction) *k*-space density for V derived from the unenhanced *p*-space density of figure 2(*a*). The straight lines show the outlines of the first BZ and the subscripts on the symmetry points define the path of integration through the zone. (*b*) The difference between the enhanced (figure 2(*c*)) and unenhanced (figure 2(*b*)) *p*-space densities for V (integrated along the 110-direction). The straight lines show the outline of the projected first BZ.

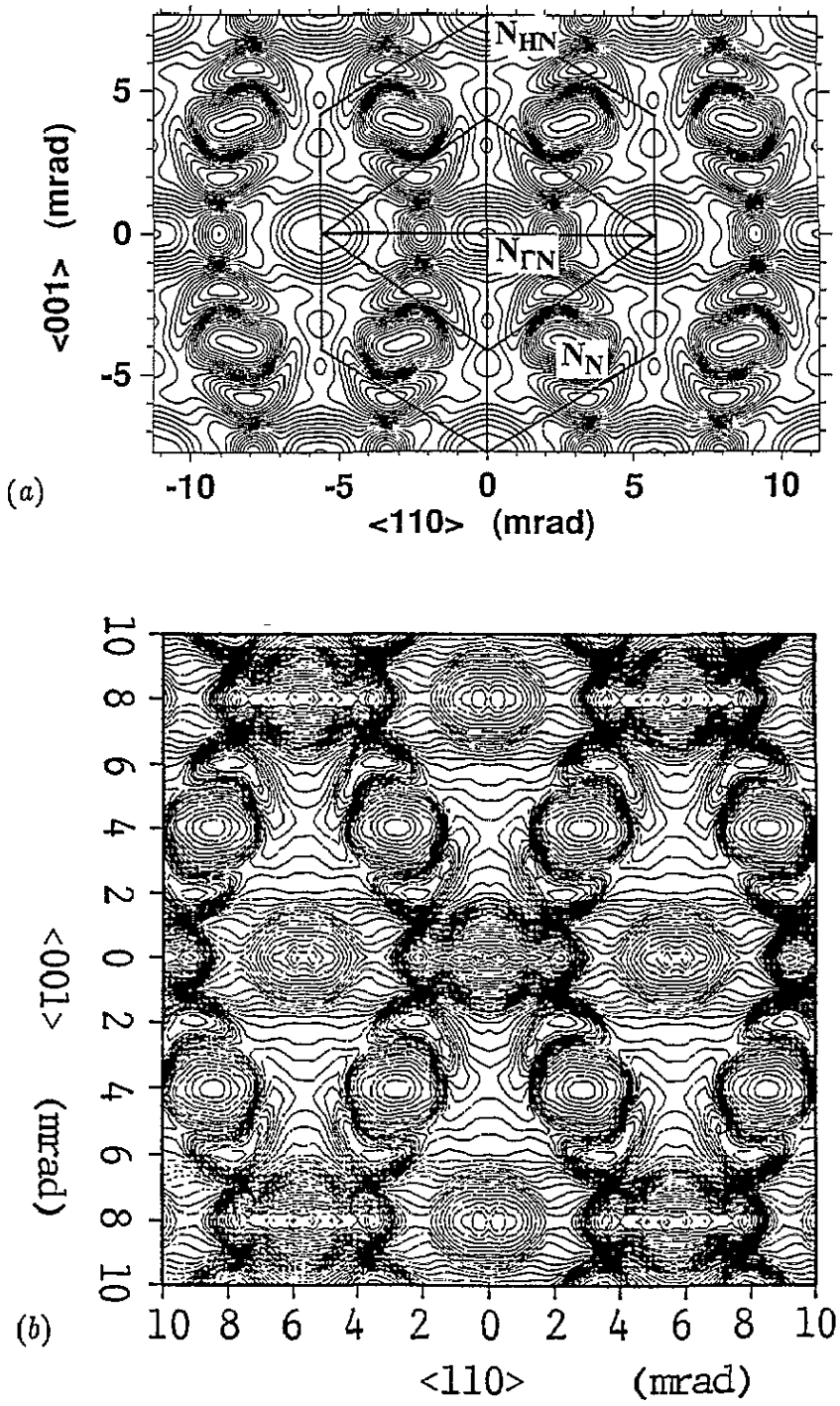

Figure 4. (*a*) A distribution arising from the difference distribution in figure 3(*b*). The notations are the same as in figure 3(*a*). (*b*) Integrated theoretical (along 110 direction) *k*-space density for V derived from the *p*-space density of figure 2(*d*).

shape to those in figure 4(*b*). The same applies to the general features at $N_{\Gamma N}$, particularly in the case of the lobes.

These preliminary results, we believe, demonstrate the possible power of such ways of analysing 2D ACAR data. Further investigations are under way to compare the experimental vanadium data with new theoretical calculations using the LMTO method and positron–electron correlations. Studies are also under way to probe the applicability of this analysis technique in positron studies of FS topologies in more complicated systems where the usual straightforward LCW folding does not produce conclusive pictures [7].

Substantial financial support from the ENEA, Bologna, Italy, Politecnico Milano, Italy, SERC, UK and The Royal Society towards this project is gratefully acknowledged. The authors would also like to thank Professor West, Professor Gyorffy, Professor Manuel and Dr Fews for illuminating discussions.

References

[1] Kajcsos Zs and Szeles Cs (ed) 1992 *Positron Annihilation (Mater. Sci. Forum)* **105–110**
[2] Dorikens L (ed) 1989 *Positron Annihilation* (Singapore: World Scientific)
Alam A *et al* (ed) 1989 *Positron Studies of Condensed Matter* (Bristol: Hilger)
[3] Berko S 1983 *Positron Solid State Physics* ed W Brandt and A Dupasquier (Amsterdam: North-Holland) p 64
[4] Lock D G, Crisp V H and West R N 1973 *J. Phys. F: Met. Phys.* **3** 561
[5] West R N, Mayers J and Walters P A 1979 *J. Phys. E: Sci. Instrum.* **14** 478
[6] Majumdar C K 1965 *Phys. Rev.* A **140** 227
Mijnarends P E, in [3] p 146
[7] Haghighi H, Kaiser J H, Rayner S J, West R N, Liu J Z, Shelton R, Howell R H, Solal F and Fluss M J 1991 *Phys. Rev. Lett.* **67** 382
[8] West R N *et al* 1993 in preparation
[9] Shanon C E and Weaver 1949 *The Mathematical Theory of Communication* (University of Illinois Press)
[10] Gull S F and Skilling J 1985 *Maximum Entropy and Bayesian Methods in Inverse Problems* ed C R Smith and W T Grandy (Dordrecht: Reidel)
[11] Matsumoto M and Wakoh S 1986 *J. Phys. Soc. Japan* **55** 3948